Asian Journal of Pharmaceutical Sciences 19 (2024) 100913

Available online at www.sciencedirect.com

ScienceDirect

journal homepage: www.elsevier.com/locate/AJPS

Research Article

Biomimetic Integrated Nanozyme for Flare and Recurrence of Gouty Arthritis

Rui Wang[a], *Tongyao Liu*[a], *Xinhong Li*[a], *Enhao Lu*[a], *Yiting Chen*[a], *Kuankuan Luo*[a], *Tao Wang*[a], *Xueli Huang*[a], *Zhiwen Zhang*[a], *Shilin Du*[b,c,*], *Xianyi Sha*[a,*]

[a] *Key Laboratory of Smart Drug Delivery (Ministry of Education), Institutes of Integrative Medicine, Department of Pharmaceutics, School of Pharmacy, Fudan University, Shanghai 201203, China*

[b] *Department of Emergency Medicine, Shanghai Geriatric Medical Center, Shanghai 201104, China*

[c] *Department of Emergency Medicine, Zhongshan Hospital, Fudan University, Shanghai 200032, China*

ARTICLE INFO

Article history:
Received 17 June 2023
Revised 17 February 2024
Accepted 26 February 2024
Available online 18 April 2024

Keywords:
Gouty arthritis
Inflammation
Nanozyme
Platinum
Prussian blue

ABSTRACT

Flare and multiple recurrences pose significant challenges in gouty arthritis. Traditional treatments provide temporary relief from inflammation but fail to promptly alleviate patient pain or effectively prevent subsequent recurrences. It should also be noted that both anti-inflammation and metabolism of uric acid are necessary for gouty arthritis, calling for therapeutic systems to achieve these two goals simultaneously. In this study, we propose a biomimetic integrated nanozyme, HMPB-Pt@MM, comprising platinum nanozyme and hollow Prussian blue. It demonstrates anti-inflammatory properties by eliminating reactive oxygen species and reducing infiltration of inflammatory macrophages. Additionally, it rapidly targets inflamed ankles through the camouflage of macrophage membranes. Furthermore, HMPB-Pt@MM exhibits urate oxidase-like capabilities, continuously metabolizing locally elevated uric acid concentrations, ultimately inhibiting multiple recurrences of gouty arthritis. In summary, HMPB-Pt@MM integrates ROS clearance with uric acid metabolism, offering a promising platform for the treatment of gouty arthritis.

1. Introduction

Gouty arthritis (GA) stands out as a prevalent form of inflammatory arthritis globally, affecting 0.68% to 3.9 % of adults in various countries. This prevalence demonstrates a noteworthy upward trend, linked to an earlier onset age associated with improved living standards [1,2]. Due to disorder of purine metabolism, high purine diets and so on, patients consistently experience elevated blood uric acid levels surpassing saturation solubility. Consequently, monosodium urate (MSU) crystallizes and locally deposits

* Corresponding authors.
E-mail addresses: du.shilin@zs-hospital.sh.cn (S. Du), shaxy@fudan.edu.cn (X. Sha).
Peer review under responsibility of Shenyang Pharmaceutical University.

https://doi.org/10.1016/j.ajps.2024.100913

in the joints, ultimately triggering localized inflammatory responses and tissue damage. Without effective and timely control, it can lead to serious complications such as nephritis, diabetes, and arteriosclerosis [1,3]. Unfortunately, the onset of GA is cyclical, typically manifesting in the early morning or midnight, marked by excruciating pain and a high recurrence rate [4]. However, a definitive cure for GA remains elusive, and current clinical interventions predominantly focus on relieving inflammation in the acute stage (such as non-steroidal anti-inflammatory drugs, glucocorticoids and colchicine) and long-term uric acid lowering therapy (such as xanthine oxidase inhibitors, uric acid excretory drugs and recombinant uric acid enzyme preparations) [5–8]. Nevertheless, the side effects of these drugs cannot be ignored [9,10], highlighting the urgent clinical need for medications that simultaneously address inflammation and uric acid.

Nanozymes possess enzyme-like activity and have seen extensive utilization in the biomedical field in recent years. Their popularity stems from high activity levels, cost-effectiveness, and storage stability [11–15]. For example, applications include the treatment of antioxidant stress through catalase (CAT) and superoxide dismutase (SOD) activities [16–21], biosensor detection based on peroxidase (POD) and glucose oxidase (Gox) activity [22–25], as well as cancer photokinetics and chemokinetics utilizing CAT and POD activity [26–30]. Reactive oxygen species (ROS), including superoxide anion radicals ($\cdot O_2^-$), hydrogen peroxide (H_2O_2) and hydroxyl radicals ($\cdot OH^-$), are partially reduced oxygen metabolites with strong oxidative capabilities. Excessive ROS oxidizes DNA, proteins and lipids at elevated concentrations [31–33]. Furthermore, the energy demand for cell metabolism sharply increases at the site of inflammation, resulting in a significant consumption of oxygen (O_2), ultimately causing hypoxia and further triggering excessive ROS production [34–37]. MSU activates local macrophages and then produces large amounts of ROS and an oxygen-deficient environment [38–42], both leading to the activation of NLRP3 inflammasome [43,44] and the NF-κB pathway [45–48]. Subsequently, activated local macrophages and endothelial cells release lots of inflammatory factors, such as IL-1β, TNF-α and CCL2, which in turn recruit macrophages and neutrophils in the bloodstream, leading to the infiltration of immune cells and inflammatory cascades. Therefore, it is imperative to eliminate excess ROS, provide enough O_2 at the site of inflammation and promptly relieve hypoxia during the treatment of GA [49,50].

In recent years, researchers have found that some nanozymes have superior urate oxidase (UOD) activity, such as Fe-N_4-C artificial peroxisome [51], platinum-group metals (Pd, Rh, Ir, Pt) [52–54] and MVSM@MIP molecularly imprinted nanozyme [55], which can be applied to the treatment of GA and hyperuricemia. The Platinum (Pt) nanozyme is a metallic material showcasing diverse catalytic activities, encompassing CAT, SOD [19,56–59], POD [60–63], UOD [52–54], ascorbate oxidase [64], polyphenol oxidase (PPO) [19,65], among others. In addition to the general advantages of nanozymes, the straightforward preparation and effective UOD-like activity of Pt nanozyme present a promising solution to the challenges associated with recombinant UOD [7,66–69]. Moreover, the metabolism of uric acid consumes O_2 and produces a byproduct, H_2O_2, consequently promoting inflammation. Despite the damage-relieving capabilities of Pt nanozyme through CAT and SOD activities, as well as the production of O_2, its small particle size restricts *in vivo* circulation time and efficacy. Therefore, a nano-delivery system based on Pt nanozyme emerges as a promising platform for the concurrent elimination of uric acid and ROS in the treatment of GA.

Expanding upon this groundwork, we developed a biomimetic integrated nanozyme, denoted as HMPB-Pt@MM, which loaded hollow Prussian blue (HMPB) with Pt nanozyme and then wrapped with macrophage membranes (MM). HMPB is widely employed in biology and medicine, enhancing the stability and diminishing the immunogenicity of Pt nanozyme. In conclusion, HMPB-Pt@MM alleviates hypoxia by eliminating ROS and providing O_2, enhancing the inflammatory microenvironment, and ultimately relieving the acute onset of gout. Moreover, HMPB-Pt@MM rapidly targets the site of inflammation and impedes the multiple recurrences of GA, which is suitable for the acute and recurrent nature of GA.

2. Materials and methods

2.1. Materials

Platinum tetrachloride ($PtCl_4$) and 2′,7′-dichlorofluorescein diacetate (DCFH-DA) were obtained from Sigma-Aldrich (St. Louis, USA). Cell counting kit-8 (CCK-8) and total superoxide dismutase assay kit with WST-8 and Hoechst 33258 were purchased from Beyotime Institution of Biotechnology (Shanghai, China). LPS, Dil and FITC were purchased from Dalian Meilun Biotechnology Co., Ltd (Dalian, China). Murine IFN-γ was purchased from PeproTech. CD86 monoclonal antibody was purchased from Thermo Fisher Scientific. Mouse IL-1β ELISA Kit was obtained from Lianke Bio. Potassium ferricyanide ($K_3[Fe(CN)_6]$), iron vitriol ($FeSO_4{\cdot}7H_2O$), sodium citrate and other reagents were purchased from Aladdin (Shanghai, China).

2.2. Cell cultures

RAW264.7 cells were cultured in high glucose DMEM medium (Gibco) supplemented with 10 % FBS (Hyclone), 100 U/ml penicillin, and 100 μg/ml streptomycin (Gibco). HUVEC cells were incubated in RPMI 1640 medium (Gibco) supplemented with 10% FBS (Hyclone), 100 U/ml penicillin, and 100 μg/ml streptomycin (Gibco). All cells were incubated in humidified atmosphere at 37 °C with 5% CO_2 for further measurements. To establish the GA model *in vitro*, medium of RAW264.7 cells was switched to serum-free high glucose DMEM medium with 500 ng/ml LPS for priming and incubated for 6 h. Then 200 μg/ml MSU was added and stimulated for 2 h. To construct M1 macrophages, RAW264.7 cells were incubated in serum-free high glucose DMEM medium with 100 ng/ml LPS + 20 ng/ml IFN-γ for 12 h and then confirmed through measurement of $CD86^+$ ratio via flow cytometry. To establish inflammatory endothelial cells, medium of HUVEC cells was

changed to serum-free RPMI 1640 medium with 100 ng/ml TNF-α, incubated for 12 h.

2.3. Animals

C57BL/6 male mice (18–22 g) and SD male rats (180–200 g) were purchased from the animal experiment center of Fudan University. All the animal experiments were carried out according to the ethical guidelines approved by the Institutional Animal Care and Use Committee (IACUC) of Fudan University. To develop GA model *in vivo*, we injected 50 μl suspension of MSU (20 mg/ml) into right ankles of C57BL/6 male mice, and 50 μl saline was injected into their left ankles as a blank control. After 8 h, the right ankles exhibited significant swelling, and the thickness ratio of the right foot to the left ranged between 1.2 and 1.9, confirming a successful GA model.

2.4. Preparation of Pt nanozyme

Pt nanozyme was prepared by sodium citrate reduction according to a published study [53]. Briefly, 100 ml $PtCl_4$ solution (0.05 mg/ml) was heated to boil, and then 10 ml sodium citrate solution (2.2 mg/ml) was added. Then, the solution changed from light yellow to brown. After cooling to room temperature, Pt nanozyme was purified via ultrafiltration and washed in distilled water.

2.5. Preparation of PB and HMPB

PB and HMPB were synthesized according to the reported method [70,71]. Briefly, PVP (3 g), $K_3[Fe(CN)_6]$ (264 mg) and 40 ml HCl (0.01 M) were mixed completely under magnetic stirring, and then reacted under 80 °C for 20 h. After aging, PB was purified through ultrafiltration and washed in distilled water. In a typical procedure, HMPB was obtained through chemical etching. PB (20 mg) and PVP (100 mg) were added to 20 ml HCl (1 M) in a Teflon vessel and then reacted for 4 h under 140 °C. After cooling to room temperature, HMPB was purified via ultrafiltration and washed in distilled water.

2.6. Preparation of MM

RAW264.7 cells were washed with cold PBS (pH 7.4) and collected in cell membrane protein extraction reagent A containing 1 % phenylmethylsulfonyl fluoride (PMSF, a protease inhibitor) at logarithmic stage. After lysed on ice for 15 min, membrane suspension was extruded through a 400 nm carbonate film repeatedly, and then centrifuged at 2,000 g for 10 min at 4 °C to collect the supernatant. Next, the supernatant was centrifuged at 14,000 g for 30 min at 4 °C to collect MM. The concentration of MM was quantified by bicinchoninic acid (BCA) protein concentration assay kit.

2.7. Preparation of HMPB-Pt and HMPB-Pt@MM

Pt nanozyme (1 ml, 1 mg/ml) was added slowly to 2 ml HMPB (1 mg/ml) under ultrasound. Subsequently, solution was gently stirred overnight and purified through centrifugation (9,000 rpm, 4 °C) for 10 min to obtain HMPB-Pt. HMPB-Pt and MM were mixed (Pt: MM = 5: 2, quality ratio), and then repeatedly extruded through 200 nm polycarbonate membrane to prepare HMPB-Pt@MM.

2.8. Characterization

The particle size distribution and zeta potential of Pt nanozyme, PB, HMPB, HMPB-Pt and HMPB-Pt@MM were determined through a laser particle size analyzer (Malvern 3600, USA). The morphologies of them were observed via TEM (Tecani, G2 S-TWIN, FEI, USA). The typical markers on macrophages of IL-1R1, CCR2 and LFA-1 were identified by western blot analysis. In order to assess stability in different media, HMPB-Pt@MM was diluted to 100 μg/ml with PBS, DMEM medium, 10% FBS+DMEM medium, 50% FBS+DMEM medium or FBS, and incubated at 4 °C for 24 h. Then centrifugated at 5,000 rpm for 10 min and observed whether there was precipitation.

2.9. Western blot analysis

Firstly, lysed cell samples via RIPA lysate and detected protein concentration by BCA. Then, protein was mixed with loading buffer and boiled for 3 min. Next, 20 μg protein of each sample was loaded on sodium dodecyl sulfate polyacrylamide gel electrophoresis (SDS-PAGE) and transferred to polyvinylidene difluoride membranes. Subsequently, the membranes were blocked with 5% skim milk in TBST for 2 h and then incubated with appropriate primary antibodies at 4 °C overnight. After washed with TBST three times, the membranes were incubated with HRP-conjugated secondary antibodies for 1 h. After washing, immunoreactive signals were visualized with increased chemiluminescence (ProteinSimple, USA) and bands were captured through the enhanced chemiluminescence detection system.

2.10. Assays of CAT-like and O_2 supplying activities

The CAT-like activity of Pt nanozyme, PB, HMPB, HMPB-Pt and HMPB-Pt@MM was assessed by measuring O_2 production, and quantified using a portable dissolved oxygen detector (Leici, China). Each system contained H_2O_2 (50 mM) in PBS buffer (pH 7.4) and various concentrations of different nanozymes, and reacted for 40 min at room temperature under magnetic stirring, continuously monitoring O_2 production at the mean time.

2.11. Assays of SOD-like activity

The SOD-like activity of Pt nanozyme, PB, HMPB, HMPB-Pt and HMPB-Pt@MM was assessed by a SOD assay kit (Beyotime, Shanghai, China) according to the standard protocol. Furthermore, we detected the $\cdot O_2^-$ scavenging ability of nanozymes via electron spin resonance (ESR). The hypoxanthine/xanthine oxidase reaction system was applied to produce $\cdot O_2^-$, and then nanozymes were added to the system. Finally, characteristic signal peak of $\cdot O_2^-$ was detected by ESR spectrometer (BRUKER A300, Germany) with BMPO as the capture agent.

2.12. Assays of ·OH- scavenging activity

The ·OH- scavenging activity of Pt nanozyme, PB, HMPB, HMPB-Pt and HMPB-Pt@MM was assessed by the salicylic acid method. ·OH- was generated via Fenton reaction between $FeSO_4{\cdot}7H_2O$ and H_2O_2, which reacted with salicylic acid to produce 2,3-dihydroxybenzoic acid, exhibiting characteristic absorption at 510 nm. To evaluate ·OH- scavenging activity, 50 μl $FeSO_4{\cdot}7H_2O$ (1.8 mM), 50 μl different nanozymes, 50 μl salicylic acid and 50 μl H_2O_2 were added sequentially to the 96-well plate and then reacted for 30 min. Finally, the absorbance of 510 nm was detected by a microplate reader. Moreover, we detected the ·OH- scavenging ability of nanozymes via ESR. The $FeSO_4/H_2O_2$ system was applied to produce ·OH-, and then nanozymes were added to the system. Finally, characteristic signal peak of ·OH- was detected by ESR spectrometer with DMPO as the capture agent.

2.13. Assays of UOD-like activity

UOD-like activity was assessed by detecting the reduction of absorbance at 290 nm (the characteristic absorption of uric acid) using an ultraviolet spectrophotometer. (1) Assays of dose-dependent UOD-like activity of Pt nanozyme: uric acid (50 μM) was mixed with different concentrations of Pt nanozymes in PBS (pH 7.4), and the system was incubated at 37 °C, 120 rpm for different periods. (2) Assays of UOD-like activity of Pt nanozyme under different pH: uric acid (50 μM) was mixed with Pt nanozyme (20 μg/ml) in PBS, and then their pH was adjusted to 2.0, 4.0, 6.0 and 8.0, respectively. Then these systems were incubated at 37 °C, 120 rpm for 12 h. (3) Assays of UOD-like activity of Pt nanozyme under different O_2 contents: uric acid (50 μM) was mixed with Pt nanozyme (10 μg/ml) in PBS, and filled them with different gas (N_2 for hypoxic group, air for control group, O_2 for oxygen-enriched group), respectively. Then these systems were incubated at 37 °C, 120 rpm for 12 h. (4) Assays of UOD-like activity of Pt nanozyme, HMPB, HMPB-Pt, HMPB-Pt@MM: uric acid (50 μM) was mixed with different nanozymes (20 μg/ml) in PBS (pH 7.4), and the system was incubated at 37 °C, 120 rpm for 12 h.

2.14. In vitro safety evaluation

RAW264.7 cells were seeded in 96-well plates at 5×10^3 cells/well and incubated overnight. Then the media was changed to fresh media with Pt nanozyme, HMPB, HMPB-Pt or HMPB-Pt@MM at various concentrations (0, 5, 10, 20, 40 μg/ml), respectively ($n = 4$). After incubating for another 24 h, the cell viability was assessed by a CCK-8 assay kit according to the protocols.

2.15. Cellular uptake and adhesion of inflammatory endothelial cells

Cellular uptake was performed in M0 macrophages and M1 macrophages using confocal laser scanning microscopy (CLSM, Carl Zeiss LSM710, Germany) and flow cytometer analysis. After incubated for 6 h under magnetic stirring, HMPB-Pt and HMPB-Pt@MM were labeled with FITC. As for quantitative analysis, macrophages were seeded in 24-well plates at 1×10^5 cells/well and incubated overnight ($n = 3$). FITC-labeled HMPB-Pt and HMPB-Pt@MM (10 μg/ml) were added to each well and incubated for 4 h. Subsequently, the cells were washed three times and collected for flow cytometer analysis (Beckman, CytoFlex S, USA). As for qualitative analysis, macrophages were seeded in confocal dishes at 5×10^5 cells/dish and incubated overnight. Next, FITC-labeled HMPB-Pt and HMPB-Pt@MM (10 μg/ml) were added to each group and incubated for 4 h. By contrast, cell membranes were labeled with Dil (10 μM) and nuclei were stained with Hoechst 33258 (5 μg/ml) for observation under CLSM.

The adhesion of inflammatory endothelia cells was examined in TNF-α-stimulated HUVEC cells by CLSM and flow cytometer analysis. And HMPB-Pt and HMPB-Pt@MM were labeled with FITC. As for quantitative analysis, HUVEC cells were seeded in 12-well plates at 2×10^5 cells/well and incubated overnight ($n = 3$). FITC-labeled HMPB-Pt and HMPB-Pt@MM (10 μg/ml) were added to each well and incubated for 10 min. Subsequently, the cells were washed three times and collected for flow cytometer analysis. As for qualitative analysis, HUVEC cells were seeded in confocal dishes at 2×10^5 cells/dish and incubated overnight. Next, FITC-labeled HMPB-Pt and HMPB-Pt@MM (10 μg/ml) were added to each group and incubated for 10 min. By contrast, cell membranes were labeled with Dil (10 μM) and nuclei were stained with Hoechst 33,258 (5 μg/ml) for observation under CLSM.

2.16. Assays of intracellular ROS

Intracellular ROS levels were measured by DCFH-DA via inverted fluorescence microscope (Leica, DMI4000D, Germany) and flow cytometer analysis. As for quantitative analysis, macrophages were seeded in 24-well plates at 1×10^5 cells/well and incubated overnight ($n = 3$). GA models were constructed on them, excluding the control group ($n = 3$). Subsequently, the media was changed to fresh media with Pt nanozyme, HMPB, HMPB-Pt or HMPB-Pt@MM (5 μg/ml), respectively, and incubated for 12 h. For the detection of ROS-scavenging ability, cells were stained with DCFH-DA for 20 min. Finally, the cells were washed three times and collected for flow cytometer analysis. In the meantime, intracellular ROS levels were qualitatively analyzed by inverted fluorescence microscope.

2.17. Assays of M1 macrophage infiltration in vitro

The degree of M1 macrophage infiltration was examined through western blot and flow cytometry analysis. Macrophages were seeded in 24-well plates at 1×10^5 cells/well and incubated overnight ($n = 3$). GA models were constructed on them except the control group ($n = 3$). Next, the media was changed to fresh media with Pt nanozyme, HMPB, HMPB-Pt or HMPB-Pt@MM (5 μg/ml), respectively, and incubated for 12 h. Subsequently, each group was incubated with anti-CD86 for 15 min and washed with PBS three times. Finally, cells were harvested and analyzed through flow cytometry. Similarly, M1 macrophage infiltration was also measured by calculating the expression of CD86 via western blot.

Table 1 – Scoring system for arthritis severity [72].

Inflammation score	External characteristics
0	No evidence of redness or swelling
1	Mild swelling confined to the paw
2	Moderate swelling and redness confined to the paw
3	Moderate swelling and redness extending from the paw to the ankle
4	Moderate swelling and redness extending from the paw to the ankle, with invisible joint features of the ankle
5	Severe swelling and redness extending from the paw to the ankle, with immovable right leg

2.18. Assays of hypoxia in vitro

The degree of hypoxia *in vitro* was measured by calculating the expression of HIF-1α in RAW264.7 cells through western blot. Cells were incubated and processed as mentioned above and then collected for western blot.

2.19. Imaging and targeting of inflammatory ankles in vivo

The targeting ability of HMPB-Pt and HMPB-Pt@MM was measured via *in vivo* imaging spectrum (IVIS) system. Firstly, we constructed GA models in mice and nanozymes were fluorescently labeled with FITC as described above. After GA models were constructed successfully, mice were divided into 3 groups ($n = 3$) and injected intravenously with free FITC, FITC-labeled HMPB-Pt or FITC-labeled HMPB-Pt@MM (1 mg/kg). To establish the targeting ability of nanozymes, we observed distribution of fluorescence at 2, 4, 8, 12, 16, 24 h post-injection via IVIS system and semi-quantify the results of the region of interest (ROI) via a Living Image Software.

2.20. Therapeutic efficacy on GA in vivo

After successful construction of GA models, mice were randomly divided into 6 groups ($n = 6$): (1) Saline, (2) Indo, (3) Pt nanozyme, (4) HMPB, (5) HMPB-Pt, (6) HMPB-Pt@MM. Formulations (3 mg/kg) in each group were intravenously injected 8 h post MSU injection. We measured the thickness of paws in each group by vernier calipers 4, 16, 24, 40, 48 h post-injection and calculated the swelling elimination rate as Eqs. (1) and (2).

$$C = \frac{the\ thickness\ of\ right\ paw}{the\ thickness\ of\ left\ paw} \tag{1}$$

$$\text{Swelling Elimination Rate (\%)} = \frac{C_{0h} - C_x}{C_{0h} - C_{-8h}} \times 100\% \tag{2}$$

$x = 4, 16, 24, 40, 48$ h

At 16 h post-injection, we recorded by photograph and evaluated the severity of inflammation according to the scoring system for arthritis severity as Table 1. Moreover, we harvested ankles of each group for hematoxylin and eosin (HE) and immunohistochemical (IHC) staining. To explore the mechanism of inhibiting relapses in GA with HMPB-Pt@MM, we collected ankles at 24 h and 48 h post-injection and quantified the Pt content using ICP-MS (PerkinElmer NexION 2000, USA).

2.21. Pharmacokinetics of Pt nanozyme and HMPB-Pt@MM in vivo

To assess the pharmacokinetics of Pt nanozyme and HMPB-Pt@MM *in vivo*, SD male rats were divided into 2 groups ($n = 3$): (1) Pt nanozyme and (2) HMPB-Pt@MM. Formulations (3 mg/kg) in each group were intravenously injected and blood samples were collected at predefined intervals (0, 1, 2, 4, 8, 12, 24, 48, 72 h). The samples were centrifuged at 10,000 rpm for 3 min and Pt content in plasma was quantified via ICP-MS. Pharmacokinetic parameters were calculated by using Excel and DAS software.

2.22. Biocompatibility in vivo

To assess the biocompatibility of HMPB-Pt@MM, main organs of healthy mice, GA model mice, as well as GA model mice with HMPB-Pt@MM injection, were dissected for HE staining. And the effect on bloodstream of HMPB-Pt@MM was assessed by hemolytic experiment. Briefly, 50 µl HMPB-Pt@MM solution of different concentrations, 600 µl red blood cell suspension (2%, v/v) and 550 µl PBS was added to tubes and mixed well. In addition, equal volumes of PBS and water were mixed with the red blood cell suspension as a negative and positive control. All of them were incubated at 37 °C for 4 h and then centrifuged at 1,500 rpm for 4 min. The supernatant was collected and the absorbance at 540 nm was detected. Hemolysis rate was calculated as Eq. (3).

$$\text{Hemolysis rate (\%)} = \frac{OD - OD_{negative}}{OD_{positive} - OD_{negative}} \times 100\% \tag{3}$$

2.23. Statistical analysis

Data are presented as the mean ± standard deviation (SD). Data analysis and comparison were calculated by Student's *t*-test and one-way ANOVA using GraphPad Prism 8.0 software (GraphPad Software Inc., La Jolla, CA, USA). Significant difference was illustrated as $P < 0.05$ and $P < 0.01$.

3. Results and discussion

3.1. Preparation and characterization of HMPB-Pt@MM

HMPB is a nanozyme with CAT-like and SOD-like activities, widely employed in the antioxidant treatment of diverse diseases. Its hollow structure provides a higher specific surface area, enhancing enzyme activity. Leveraging these characteristics, we load Pt nanozyme into HMPB and coat HMPB-Pt with MM, constructing a biomimetic integrated nanozyme system HMPB-Pt@MM. The preparation of HMPB-Pt@MM was divided into 4 steps (Fig. 1A): (I) PB was prepared

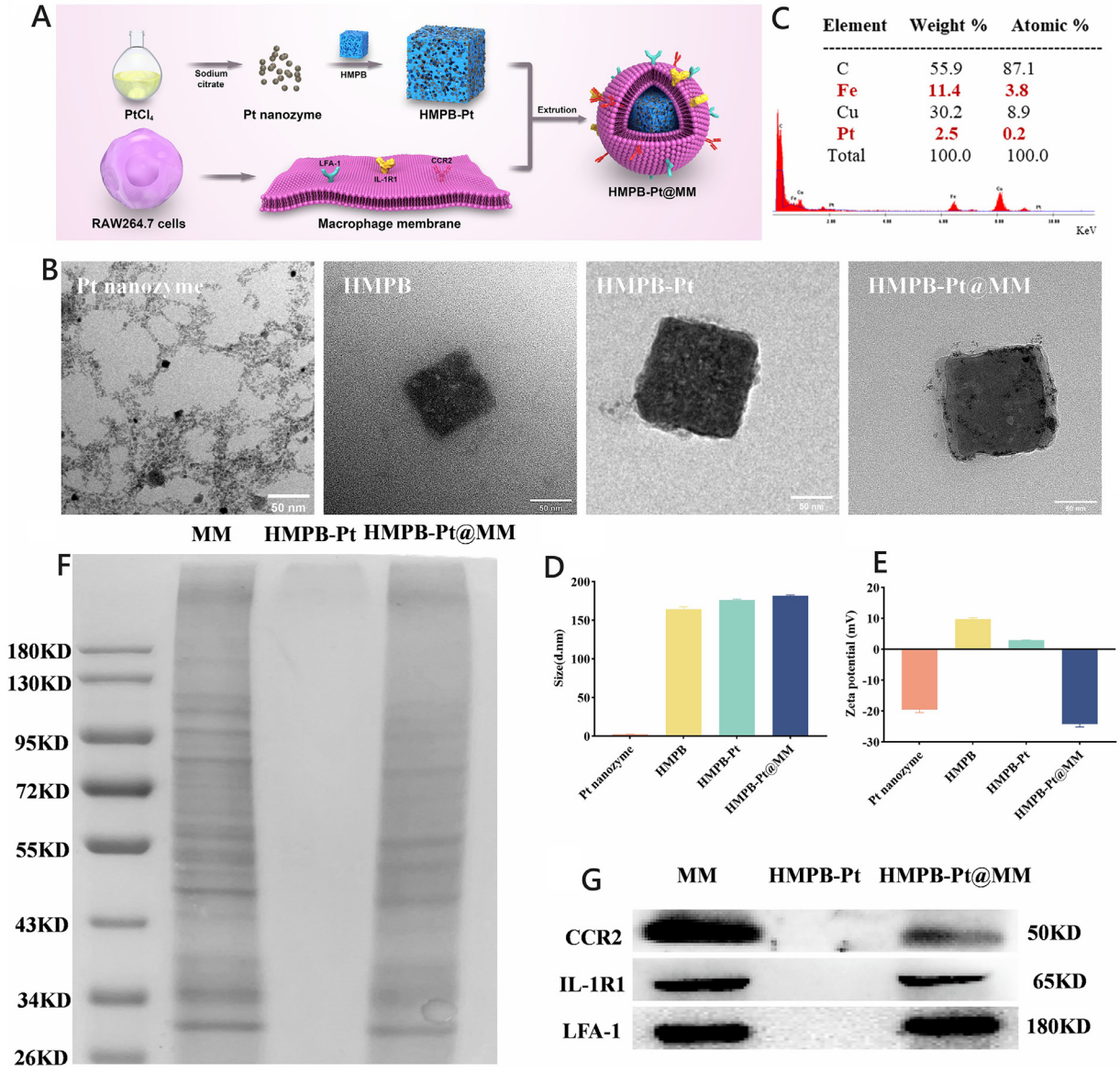

Fig. 1 – Fabrication and characterization of HMPB-Pt@MM. (A) Construction of HMPB-Pt@MM; (B) TEM images of Pt nanozyme, HMPB, HMPB-Pt and HMPB-Pt@MM, respectively; scale bar = 50 nm; (C) EDS results of HMPB-Pt; (D) Particle sizes and (E) zeta potentials; (F) SDS-PAGE result proved the integrity of cell membrane proteins; (G) Western blot analysis showed the representative protein bands of CCR2, IL-1R1 and LFA-1. Data are presented as mean ± SD (*n* = 3).

via thermal aging reaction using potassium ferricyanide and polyvinylpyrrolidone as raw materials and then etched into HMPB in acid solution at 140 °C via reactor. (II) Sodium citrate was used to reduce platinum tetrachloride to Pt nanozyme via green chemical reduction method. (III) HMPB-Pt was constructed via electrostatic adsorption after stirring HMPB and Pt nanozyme overnight. (IV) MM was isolated via cell membrane extraction kit, and then extruded with HMPB-Pt through a 200 nm carbonate film repeatedly, so that MM was coated on the surface of HMPB-Pt. Transmission electron microscopy (TEM) results showed that Pt nanozyme exhibited uniform spherical shape of 2.49 nm (Fig. 1B) with a lattice size of 0.123 nm (Fig. S1). PB was a square nanoparticle of 256.07 nm, and the size of HMPB reduced to 164.40 nm after etching, due to the surface corrosion of PB under high temperature and high concentration of acid. Along with that, a distinct mesoporous structure was observed within the HMPB. The particle size of HMPB-Pt increased to 176.20 nm due to the Pt nanozyme binding to HMPB. The size of HMPB-Pt@MM increased to 181.77 nm after coating with MM, and MM layer on the surface was visible through TEM. Energy dispersive X-ray spectrum (EDS) results (Fig. 1C) revealed a mass ratio of iron to platinum in HMPB-Pt of 4.56:1. The results of dynamic light scattering (DLS) analysis in Fig. 1D and 1E also demonstrated the sizes and zeta potentials of particles. The size of particles

measured by DLS was larger than TEM because DLS measured hydrodynamic particle size, while TME measured the size of dry particles. It is worth mentioning that the hydrated particle size of Pt nanozyme was 136.76 nm, possibly because of agglomeration in the solution. After HMPB-Pt extruded with MM, the zeta potential ranged from −2.0 to −12.2 mV, closing to the potential of MM, and indicating the successful camouflage of MM. In addition, the integrity of cell membrane proteins was proved by SDS-PAGE (Fig. 1F), also demonstrating successful camouflage of MM. As shown in Fig. S7, there was no precipitation in all of the tubes after incubation for 24 h, indicating good stability of HMPB-Pt@MM in various media. At the same time, Western blot (Fig. 1G) analysis demonstrated the presence of IL-1R1 (the receptor for IL-1β), CCR2 (the receptor for monocyte chemoattractant protein-1 (MCP-1)), and lymphocyte function-associated antigen (LFA-1, the receptor for intercellular cell adhesion molecule-1 (ICAM-1)) on the MM surface. In addition to providing inflammation-targeting property with nanoparticles, MM layers may also alleviate inflammation by binding to inflammatory factors via receptors on the surface [73–75].

3.2. *ROS scavenging and O_2 supplying of HMPB-Pt@MM*

As it is well-known, bursts of ROS induce oxidative stress and contribute to various diseases [73,74]. H_2O_2 is a metabolic byproduct capable of permeating cell membranes, displaying high cytotoxicity. H_2O_2 could be catalyzed by CAT into H_2O and O_2, thus we measured CAT-like activity as well as O_2 production capacity by detecting dissolved O_2 in solution via a portable dissolved oxygen detector. As shown in Fig. 2A, the bubbles in the solution indicated the production of O_2. The highly active surface of Pt nanozyme imparts significant CAT-like activity at low doses, leading to the rapid production of a large amount of O_2 within 1 min in pH 7.4 solution (Fig. S2). The CAT-like activity of Pt nanozyme was 2.5 times higher than that of HMPB at an equivalent dose. However, the rapid production of large amounts of O_2 may not be beneficial and could lead to oxidative damage to cells [76–78]. To address this dilemma, we loaded HMPB with Pt nanozyme to decrease the rate of O_2 production without affecting the total amount (Fig. 2B). After 10 min, HMPB-Pt@MM (10 μg/ml) produced 26.15 mg/l of dissolved O_2, increasing to 35.47 mg/l after 40 min. The above results proved that HMPB-Pt@MM not only scavenged H_2O_2 but also produced O_2, alleviating the local hypoxic environment of inflammation. $\cdot O_2^-$ serves as a precursor to the majority of other ROS and participates in the propagation of oxidative chain reactions, also known as the “initiator” of ROS bursts [79–81]. When the production and clearance of $\cdot O_2^-$ are out of balance, it may lead to diseases. SOD enzymes are natural scavengers of $\cdot O_2^-$ in the body, and their mimics have been used in the treatment of various diseases, such as ischemic stroke [82–84], arthritis [85–87], inflammatory bowel disease [88–90] and so on. We fabricated $\cdot O_2^-$ by the catalytic reaction of xanthine oxidase, which then combined with WST-8 to produce a formazan dye that could be measured by a microplate reader at 450 nm to exhibit SOD-like activity. As shown in Fig. S3, SOD-like activity of Pt nanozyme and HMPB both increased in a dose-depended manner. While SOD-like activity of Pt nanozyme was significantly higher than that of HMPB, about 3 folds of it. As shown in Fig. 2C, HMPB-Pt@MM (10 μg/ml) metabolized 44.62% of total $\cdot O_2^-$, slightly less than HMPB-Pt (52.84%), possibly due to the MM layer. Next, we evaluated the $\cdot OH^-$ scavenging activity of nanozymes based on the reaction between $\cdot OH^-$ and salicylic acid, whose product (2,3-dihydroxybenzoic acid) has characteristic absorption at 510 nm. With the addition of Pt nanozyme, HMPB, HMPB-Pt or HMPB-Pt@MM, the absorbance at 510 nm significantly reduced, demonstrating their $\cdot OH^-$ scavenging activity (Fig. S4 and 2D). Approximately 35% of $\cdot OH^-$ was removed by HMPB-Pt@MM (10 μg/ml) and 31.42% by HMPB-Pt (10 μg/ml). We simultaneously employed ESR to confirm the ROS scavenging activity of nanozymes. Characteristic peak signals of $\cdot O_2^-$ and $\cdot OH^-$ both decreased obviously with the addition of different nanozymes, especially Pt nanozyme at the same concentration (Fig. 2G and 2H). Above results proved that HMPB-Pt@MM has excellent ROS scavenging and O_2 supplying capacity, exhibiting potential as an anti-oxidative stress platform.

3.3. *Uric acid metabolizing of HMPB-Pt@MM*

When a high concentration of uric acid precipitates and deposits in joints, inflammation occurs, initiating GA [1]. Indeed, UODs such as rasburicase and pegloticase have been employed in the treatment of GA, but their clinical application is constrained by poor physicochemical properties, strong immunogenicity, and high costs [91]. Surprisingly, Pt nanozyme has demonstrated UOD-like activity and is expected to address the challenges associated with them. We assessed UOD-like activity by measuring the reduction in absorbance of uric acid at 290 nm and found that 10 μg/ml Pt nanozyme metabolized nearly 50 μM uric acid in 24 h (Fig. 2F). It is worth noting that the decomposition of uric acid also produced H_2O_2, which could be eliminated by the CAT-like activity of HMPB-Pt@MM. Therefore, the combination of Pt nanozyme and HMPB was intelligent and useful. To explore whether O_2 affects UOD-like activity, we investigated it under oxygen-rich, hypoxia, and normal conditions (Fig. S5), and found that UOD-like activity was significantly reduced under hypoxia, reaching nearly 50% of that in oxygen-enriched conditions. Thanks to the CAT-like activity, HMPB-Pt@MM itself could continuously produce O_2, thereby promoting the decomposition of uric acid. Additionally, we assessed the UOD-like activity at different pH levels (Fig. S6), and Pt nanozyme maintained more than 95% UOD-like activity over a wide pH range of 4.0 to 8.0, making it suitable for implementation *in vitro* and *in vivo*. As shown in Fig. 2E, HMPB had no UOD activity, but HMPB-Pt enhanced the UOD-like activity of Pt nanozyme, leading to the complete metabolism of 50 μM uric acid in 12 h. Although the rate of uric acid decomposition by HMPB-Pt@MM slightly decreased in the first 10 h due to the presence of MM layer, 50 μM of uric acid completely metabolized after 12 h, and there was still 5.79% of uric acid left in Pt nanozyme group at the same time. In conclusion, HMPB-Pt@MM not only decomposed locally high concentrations of uric acid but also reduced ROS and supplied O_2, thereby alleviating oxidative stress in GA.

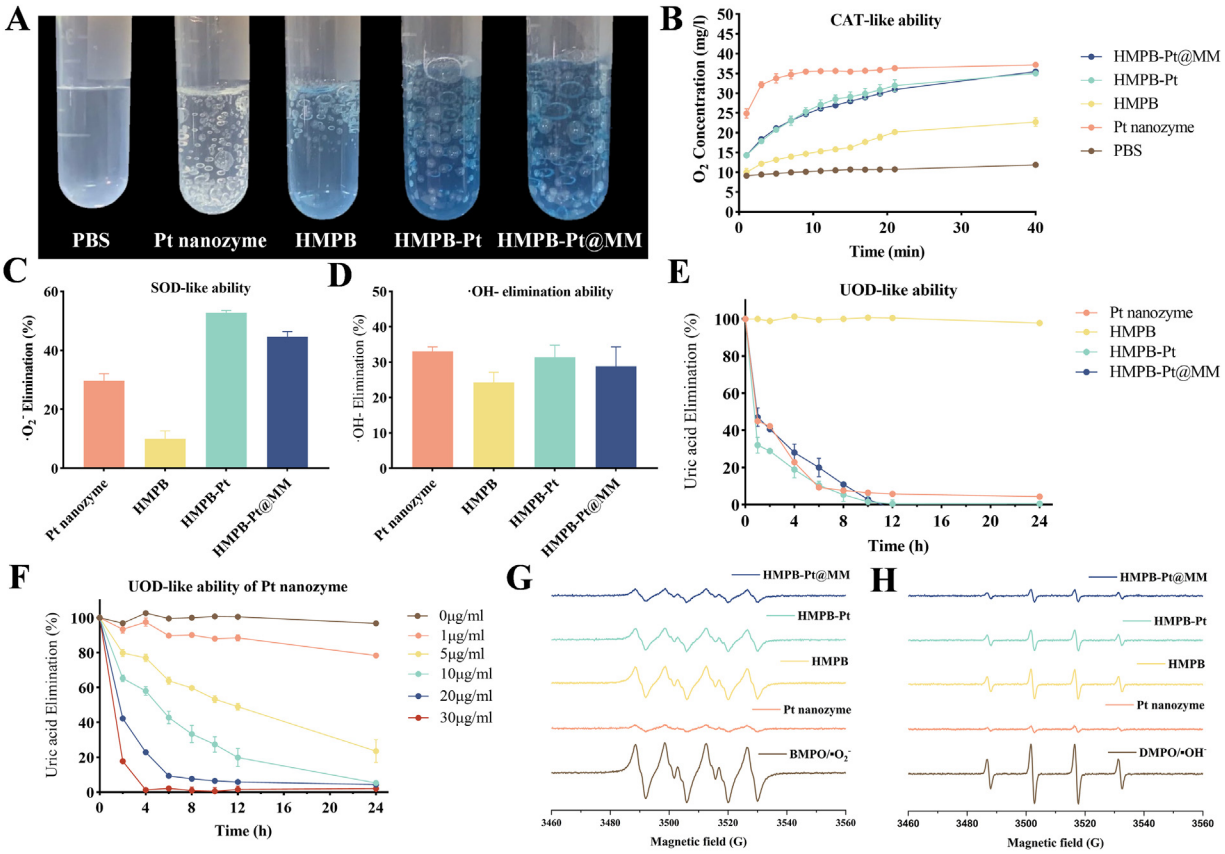

Fig. 2 – Multiple enzyme activities of HMPB-Pt@MM. (A) Bubbles in the solution indicated the production of O_2; (B) CAT-like ability of Pt nanozyme, HMPB, HMPB-Pt and HMPB-Pt@MM (10 μg/ml) was assessed by the yield of O_2; (C) SOD-like ability of different nanozymes (10 μg/ml) was assessed by kit; (D) $\cdot OH^-$ elimination ability of different nanozymes (10 μg/ml) was assessed via reaction of salicylic acid with $\cdot OH^-$; (E) UOD-like activity of different nanozymes was assessed through the metabolism of uric acid; (F) Dose-dependent UOD-like activity of Pt nanozyme; (G) $\cdot O_2^-$ scavenging property of different nanozymes (10 μg/ml) by ESR; (H) $\cdot OH^-$ scavenging property of different nanozymes (10 μg/ml) by ESR. Data are presented as mean ± SD (n = 3).

3.4. *HMPB-Pt@MM inhibited oxidative stress and hypoxia in vitro, and reduced inflammatory macrophage infiltration*

Upon MSU stimulation, resident macrophages initiate inflammation, followed by the recruitment and conversion of monocyte-derived macrophages into M1 macrophages, thereby exacerbating the inflammatory response [92–94]. We first evaluated the safety of Pt nanozyme, HMPB, HMPB-Pt, and HMPB-Pt@MM on RAW264.7 macrophages. As shown in Fig. 3A, none of them exhibited cytotoxicity up to 40 μg/ml, indicating excellent biocompatibility. Subsequently, we compared cellular uptake of HMPB-Pt and HMPB-Pt@MM by macrophages via CLSM and flow cytometry. Fluorescein isothiocyanate isomer (FITC), a green fluorescence dye, was labeled with them. M1 macrophages were successfully induced by LPS and IFN-γ using a typical method, confirmed by measuring the $CD86^+$ ratio via flow cytometry (Fig. S8). As shown in Fig. 3B, strong green fluorescence was found in M1 macrophages incubated with HMPB-Pt@MM, indicating the uptake efficiency of HMPB-Pt@MM in M1 macrophages was significantly higher than HMPB-Pt. This conclusion was also confirmed by quantitative analysis results (Fig. 3D), the uptake efficiency of HMPB-Pt@MM was 1.17-fold of HMPB-Pt. Interestingly, we observed that the MM camouflage promoted cellular uptake by M1 macrophages and evasion from the reticuloendothelial (RES) system , resulting in a 3.45-fold increase in cellular uptake by M1 macrophages compared to M0 macrophages. We hypothesized that the difference in the uptake of HMPB-Pt@MM by macrophages of different phenotypes was attributed to the expression of certain proteins. On the one hand, ICAM-1 and TLR4 are up-regulated in M1 macrophages. ICAM-1 on M1 macrophages binds to LFA-1 on the surface of HMPB-Pt@MM (Fig. 1G), and TLR4 promotes the uptake of HMPB-Pt@MM by M1 macrophages. On the other hand, CD47, the self-marker of most cells, inhibits phagocytosis by binding to signal regulatory protein α (SIRPα) of macrophages, transmitting the signal of "don't eat me", thereby reducing the uptake of HMPB-Pt@MM by M0 phenotype [95]. However, the expression of SIRPα is reduced in M1 macrophages, thus alleviating "phagocytic inhibition" [96]. Because of these two reasons, HMPB-Pt@MM was taken

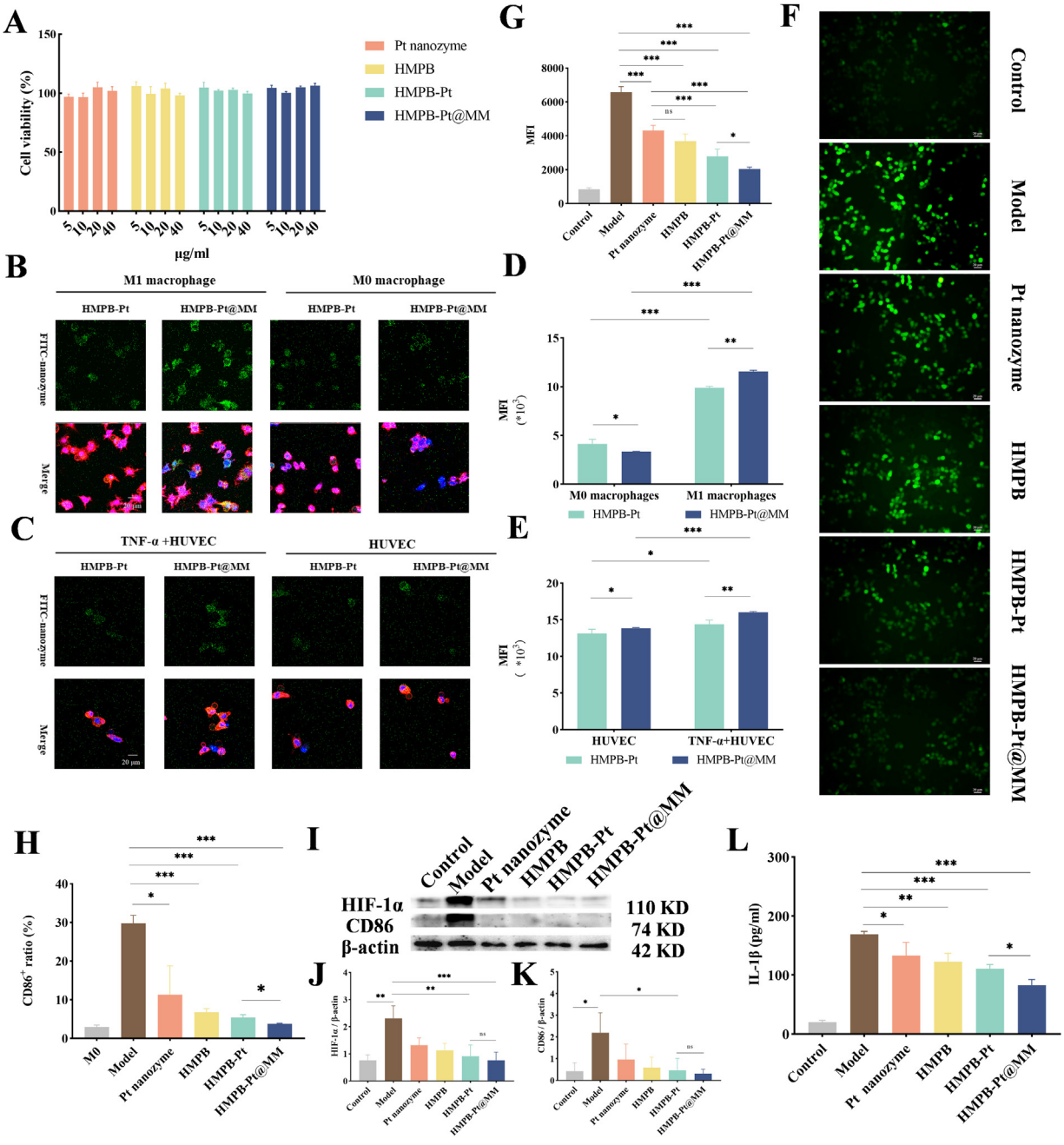

Fig. 3 – HMPB-Pt@MM targeted M1 macrophages and reduced inflammation *in vitro*. (A) Biocompatibility of different nanozymes *in vitro*; (B) Cellular uptake of HMPB-Pt or HMPB-Pt@MM in M1 and M0 macrophages by CLSM imaging; scar bar = 20 μm; (C) Cellular adhesion of HMPB-Pt or HMPB-Pt@MM in HUVEC by CLSM imaging; scar bar = 20 μm; (D) Quantification of cellular uptake of HMPB-Pt or HMPB-Pt@MM in M1 and M0 macrophages by measuring the mean fluorescence intensity (MFI) with flow cytometer analysis; (E) Quantification of cellular adhesion of HMPB-Pt or HMPB-Pt@MM in HUVEC by measuring the MFI with flow cytometer analysis; (F) ROS-eliminating effects in each group by fluorescence imaging; scar bar = 20 μm; (G) Quantification of ROS-eliminating effects in each group by flow cytometer analysis; (H) Proportion of M1 macrophages in each group; (I) Western blot analysis showed HIF-1α and CD86 levels in each group; (J) Semi-quantitative analysis of HIF-1α expression levels in each group; (K) Semi-quantitative analysis of CD86 expression levels in each group; (L) IL-1β levels in the supernatants of each group by ELISA kit. Data are presented as mean ± SD (n = 3); ns = not significant, *P < 0.05, **P < 0.01 and ***P < 0.001.

up more by M1 macrophages and less by M0 macrophages. Besides, LFA-1 on the surface of MM could adhere to ICAM-1, which was highly expressed on inflammatory endothelial cells, endowing inflammatory targeting effects with HMPB-Pt@MM [97,98]. We induced the inflammatory phenotype of endothelial cells using TNF-α, and as anticipated, more HMPB-Pt@MM adhered to inflammatory endothelial cells compared to HMPB-Pt (Fig. 3C and 3E). Taken together, the camouflage of MM conduced to target inflammatory site and M1 macrophages, as well as escaping from RES system.

Next, we primed RAW264.7 cells with 500 ng/ml LPS for 6 h and then stimulated with 200 μg/ml MSU for 2 h to establish the model of GA *in vitro* [99–102]. We assessed the ROS level of GA model *in vivo* via DCFH-DA, a typical probe for ROS detecting. As shown in Fig. 3F and 3G, strong green fluorescence signals were observed in the group of GA model, indicating high expression of ROS, approximately 7.84-fold of control group. After incubated with Pt nanozyme, HMPB, HMPB-Pt or HMPB-Pt@MM, the fluorescence signals of ROS decreased to different extents, respectively 68%, 56%, 42% and 31% of GA model group. Among them, HMPB-Pt@MM minimized 2.22-fold the expression of ROS over model group, possibly owing to the increased cellular uptake.

In an environment abundant in inflammatory factors and ROS, macrophages tend to exhibit proinflammatory M1 phenotype, characterized by the typical marker CD86. We assessed the therapeutic effect of HMPB-Pt@MM on macrophage polarization via flow cytometry. As shown in Fig. 3H, the GA model group had approximately 29.83% M1 macrophages. Upon incubated with different nanozyme groups, the percentage of M1 macrophages decreased significantly, reaching only 3.80% in the HMPB-Pt@MM group, nearly 6.85-fold lower than the model group and similar to the control group. At the same time, we also confirmed this conclusion via Western blot analysis (Fig. 3I and 3K). Hypoxia is another characteristic of GA and exaggerates inflammation. Hypoxia-inducible factor-1 (HIF-1) is an important transcriptional regulator that mediates cell responses to hypoxia. Its active subunit, HIF-1α, regulates oxygen metabolism and has been targeted in various inflammatory conditions [36,103–106]. We evaluated the expression of HIF-1α in different groups via Western blot, and semi-quantitative results (Fig. 3J) showed a significant increase in the GA model group and an obvious decrease in HMPB-Pt@MM group, almost the same as control group. It could be seen that HMPB-Pt@MM effectively alleviated the inflammatory hypoxia state, according to excellent O_2-supplying ability. IL-1β is a key mediator in GA and serves as "initiator" [93], triggering the subsequent inflammatory cascade. We used ELISA to assess the content of IL-1β in the cell supernatant of each group. Predictably, IL-1β was significantly reduced in the HMPB-Pt@MM group, which was 49.13% of the model group. In summary, HMPB-Pt@MM enhanced the cellular uptake of M1 macrophages and subsequently reprogrammed them to the M0 phenotype, leading to reduced expression of ROS and IL-1β and ultimately alleviating inflammation. Moreover, HMPB-Pt@MM improved hypoxic environment through O_2 supply, facilitating the restoration of redox homeostasis.

3.5. *HMPB-Pt@MM targeted the site of inflammation quickly*

During the development of inflammation, macrophages are recruited to the inflammatory site in response to a chemokine gradient. Based on this, camouflage of MM has been widely applied in biomimetic nano-drug delivery systems as an effective targeting strategy. Initially, we injected 50 μl suspension of MSU into the right ankles of C57BL/6 male mice to construct GA models, while the same volume of saline was injected into their left ankles as a blank control. After 8 h, the right paw of mice showed significant swelling, confirming the successful construction of the GA model [100,106]. Next, we investigated the biodistribution of HMPB-Pt and HMPB-Pt@MM in GA model via IVIS system. As shown in Fig. 4A and 4B, clear fluorescence signals of HMPB-Pt@MM were observed in the right ankles 2 h post-injection, surpassing those in their left ankles and in the HMPB-Pt group. At following time points, HMPB-Pt@MM consistently accumulated more in the right ankles, peaking at 4 h post-injection, nearly 1.59-fold of HMPB-Pt group, demonstrating productive inflammation targeting ability after being camouflaged with MM. In HMPB-Pt group, fluorescence signals in the left and right ankles were similar, accumulating at inflammatory site mainly due to their increased vascular permeability. After 24 h post-injection, HMPB-Pt and HMPB-Pt@MM were primarily distributed in the liver and kidney. Additionally, HMPB-Pt@MM consistently accumulated more than HMPB-Pt due to its long-circulating ability with MM modification (Fig. S9). Collectively, these results strongly demonstrated that HMPB-Pt@MM quickly targeted ankles with inflammation due to the combination of LFA-1 on the surface of HMPB-Pt@MM and ICAM-1 on inflammatory endothelial cells [75,107–109]. GA often flares suddenly and painfully, thus rapid targeting ability of HMPB-Pt@MM may relieve the pain and mitigate the progression of inflammation in time.

3.6. *HMPB-Pt@MM effectively relieved acute GA in mice*

Building on predominant anti-inflammatory ability *in vitro* and inflammation targeting characteristic *in vivo*, we further examined the therapeutic effects of different formulations (saline, indomethacin (Indo), Pt nanozyme, HMPB, HMPB-Pt, HMPB-Pt@MM) on GA mice. As shown in Fig. 4D, we constructed GA models 8 h before administering formulations, with their right paws showing obvious swelling 8 h post MSU and peaking after 12 h. We administered different formulations intravenously (3 mg/kg) to successful GA models (the thickness ratio of the right paw to the left was from 1.20 to 1.90). Next, we measured the thickness of paws in each group ($n = 6$) by vernier calipers 4 h and 16 h post-injection, and calculated the swelling elimination rate of each mouse to assess the potential anti-inflammatory effects of nanozymes. As shown in Fig. 4E, the swelling of right paws in control group and Indo group continued to increase at 4 h post-injection, albeit with a slight reduction in the Indo group compared to the model group. Compared with them, the swelling of right paws in Pt nanozyme, HMPB and HMPB-Pt groups alleviated to some extent, with reductions of 11.35%,

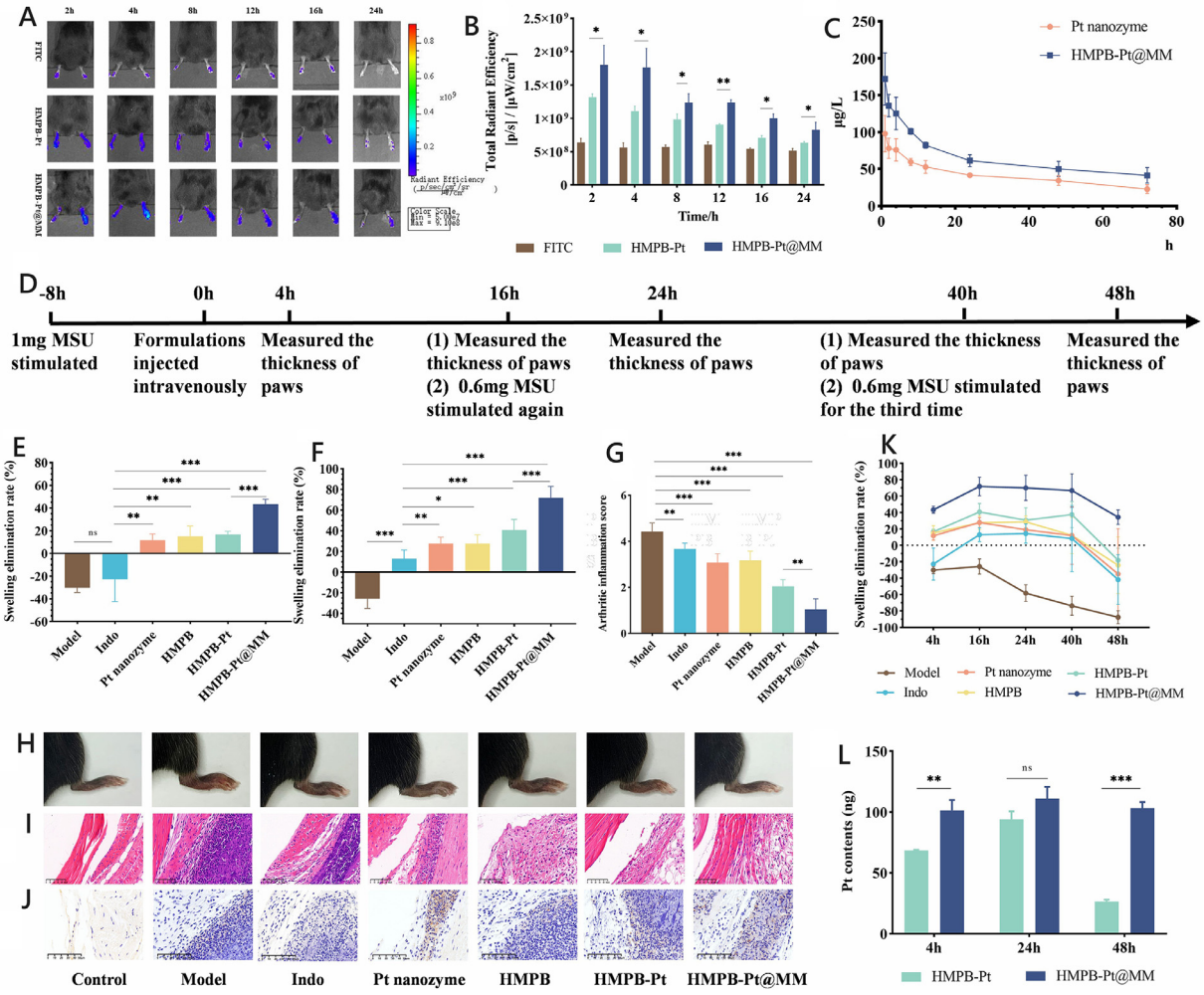

Fig. 4 – HMPB-Pt@MM effectively targeted inflammation and relieved acute GA. (A) *In vivo* imaging of FITC, FITC-labeled HMPB-Pt, and FITC-labeled HMPB-Pt@MM in GA mice at different time points post-injection; (B) Calculated fluorescence intensity in right ankles of GA mice in (A) ($n = 3$); (C) Pt plasma concentration after intravenous injection of Pt nanozyme and HMPB-Pt@MM ($n = 3$); (D) Schematic illustration of pharmacodynamic experiment protocol in GA mice; (E) Swelling elimination rate in each group at 4 h post-injection showed quick therapeutic effects of GA ($n = 6$); (F) Swelling elimination rate in each group at 16 h post-injection ($n = 6$); (G) Arthritic inflammation score in each group at 16 h post-injection according to the scoring system for arthritis severity ($n = 6$); (H) Photographs of right ankles in each group at 16 h post-injection visually indicated the level of swelling; (I) HE staining of right ankles in each group showed infiltration of immune cells; scale bar = 50 μm; (J) CD86 IHC study of right ankles in each group indicated infiltration level of M1 macrophages; (K) Swelling elimination rate in each group at different time points post-injection showed therapeutic effects of GA for flares and relapses; (L) Pt contents of right ankles in the group of HMPB-Pt and HMPB-Pt@MM at different time points post-injection ($n = 3$). Data are presented as mean ± SD; ns = not significant, *$P < 0.05$, **$P < 0.01$ and ***$P < 0.001$.

16.33% and 18.50%, respectively, at 4 h post-injection. To our surprise, HMPB-Pt@MM exhibited excellent therapeutic effects in rapid treatment of GA, which reduced the degree of swelling by 47.04% only 4 h post-injection, consistent with their quick inflammation targeting ability *in vivo*. It also demonstrated that Indo, a non-steroidal anti-inflammatory drug commonly used for GA, could not relieve the acute inflammation of GA promptly. As a small molecule drug with poor physicochemical properties, Indo does not have an inflammation-targeting ability, limiting its therapeutic effect. After 16 h of administration, Indo showed slightly anti-inflammatory effect and reduced swelling degree by 12.35% (Fig. 4F). However, other nanozyme groups illustrated better therapeutic effects in GA. As mentioned above, Pt nanozyme metabolized uric acid and different kinds of ROS, but its size was so small that it easily cleared out, showing limited efficacy and reducing the swelling only by 27.84%. HMPB, with a suitable particle size for passive targeting, reduced swelling by 28.99%, primarily through the mechanism of ROS clearance. Compared with them, HMPB-Pt combined these two nanozymes and solved the application dilemma, greatly improving the swelling elimination rate to 41.67%, nearly

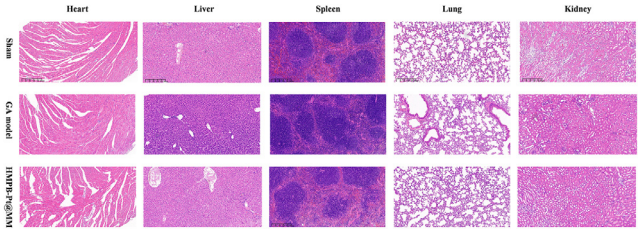

Fig. 5 – Biocompatibility of HMPB-Pt@MM *in vivo*. HE staining of main organs in the group of control, GA model, and HMPB-Pt@MM; scale bar: 200 μm.

1.44-fold of them. Surprisingly, HMPB-Pt@MM eliminated 74.38% of swelling, demonstrating a robust therapeutic effect on GA. We speculated that the superior therapeutic effect of HMPB-Pt@MM was attributed to excellent active targeting capability and the combined mechanism of uric acid degradation as well as ROS clearance. Moreover, we also photographed and evaluated severity of inflammation according to the scoring system for arthritis severity (Fig. 4H and 4G) and confirmed the above conclusions. As is known to us, lots of immune cells, such as neutrophils and monocytes, are recruited to the site of inflammation and may further cause irreversible damage without being controlled in time. To better evaluate the therapeutic effects, we collected right ankles of each group 16 h post-injection and assessed infiltration of immune cells via HE staining (Fig. 4I). Infiltration of immune cells was obviously inhibited after treatement with different formulations, especially for the group of HMPB-Pt@MM, which was nearly at a normal level. And CD86 IHC study (Fig. 4J) showed HMPB-Pt@MM significantly reduced the number of M1 macrophages, in line with results *in vitro*. Collectedly, we speculated that the superior therapeutic effect of HMPB-Pt@MM was attributed to excellent active targeting capability and the combined mechanism of uric acid degradation as well as ROS clearance. After reaching the inflamed ankles, HMPB-Pt@MM inhibited recruitments of immune cells and reprogrammed M1 macrophages into M0 phenotype, finally efficiently alleviating the flaresx of GA.

3.7. *HMPB-Pt@MM effectively inhibited the relapses of GA*

Apart from acute attacks, GA is marked by high recurrence rates. There are plenty of triggers of relapses, such as high-purine diet, alcohol intake, joint trauma, and so on. The interval between attacks gets shorter and shorter as GA progresses, and the inflammation keeps getting worse, finally destroying the joints permanently [1,110]. Building on these features, we further assessed whether a single administration of HMPB-Pt@MM could inhibit GA relapses. As shown in Fig. 4D, we re-stimulated right ankles with low doses of MSU 24 h and 48 h after the first stimulation of MSU to mimic multiple recurrences. Generally, right ankles swelled seriously 8 h post MSU stimulation, just as GA model group suggested. Taking the degree of swelling 8 h after the first stimulation of MSU as a base point, we calculated the swelling elimination rate 8 h post the second stimulation and third stimulation. As shown in Fig. 4K, the swelling of right paws increased sharply after the second and third stimulation of MSU, about 1.55-fold and 1.88-fold of that after first stimulation, respectively. These results were consistent with the clinical observation of increased severity after relapses. Fortunately, the administration of Indo, Pt nanozyme, HMPB, HMPB-Pt, and HMPB-Pt@MM did not exacerbate the degree of swelling due to the second MSU stimulation. Instead, they decreased by 18.18%, 19.08%, 28.82%, 30.77% and 70.12%, respectively. Among them, HMPB-Pt@MM showed excellent ability to inhibit relapses. Nevertheless, after the third stimulation, the swelling of all groups except HMPB-Pt@MM improved. To explore mechanism of that, we measured the Pt content of right ankles 24 h and 48 h post-injection by inductively coupled plasma mass spectrometry (ICP-MS) to assess the retention of HMPB-Pt or HMPB-Pt@MM. As shown in Fig. 4L, the Pt retention in right ankles of HMPB-Pt@MM group was 111.23 ng (equivalent to 0.56 μg HMPB-Pt@MM) 24 h post-injection, 1.18-fold of that in HMPB-Pt group. There was 103.35 ng Pt in right ankles of HMPB-Pt@MM group 48 h post-injection, 2.9-fold higher than HMPB-Pt group. We hypothesized that the high retention capacity of HMPB-Pt@MM was due to the interaction of MM with inflammation endothelial cells. Additionally, we examined the pharmacokinetics of Pt nanozyme and HMPB-Pt@MM *in vivo*, and result showed that $T_{1/2}$ of HMPB-Pt@MM was 1.62-fold higher, compared to that of Pt nanozyme (81.211 h *vs* 50.217 h). In the meantime, HMPB-Pt@MM exhibited a 1.66-fold higher AUC_{0-72} (4817.367 *vs* 2894.354 ug/$L \times h$) than Pt nanozyme (Fig.4C and Table S1). These results verified that the ability of HMPB-Pt@MM to inhibit recurrence may be due to high retention in inflammatory ankles and long-circulating ability.

3.8. *Biocompatibility of HMPB-Pt@MM in vivo*

Main organs were collected from mice in the control group, GA model group, and HMPB-Pt@MM group 48 h post-injection to assess biocompatibility through HE staining. HE staining of main organs (Fig. 5) showed no signs of toxicity related to HMPB-Pt@MM. In addition, the hemolysis rate of HMPB-Pt@MM ranged from 10 to 200 μg/ml, which was less than 1% (Fig. S10), also indicating its safety as a therapeutic platform for GA.

4. Conclusion

In summary, we developed a biomimetic integrated nanozyme, HMPB-Pt@MM, demonstrating significant capabilities in uric acid metabolism and ROS elimination. Upon administration to mice with GA, HMPB-Pt@MM rapidly targeted the site of inflammation, effectively alleviating GA flares and inhibiting relapses *in vivo*. These findings highlight the potential of HMPB-Pt@MM as a promising platform for the treatment of GA.

Conflicts of interest

The authors declare no conflict of interest.

Acknowledgments

This work was supported by the National Key R&D Program of the Ministry of Science and Technology (2022YFC2304303).

Supplementary materials

Supplementary material associated with this article can be found, in the online version, at doi:10.1016/j.ajps.2024.100913.

References

[1] Dalbeth N, Gosling AL, Gaffo A, Gout Abhishek A. Lancet 2021;397:1843–55.
[2] Dehlin M, Jacobsson L, Roddy E. Global epidemiology of gout: prevalence, incidence, treatment patterns and risk factors. Nat Rev Rheumatol 2020;16:380–90.
[3] Dalbeth N, Choi HK, Joosten LAB, Khanna PP, Matsuo H, Perez-Ruiz F, et al. Gout Nat Rev Dis Primers 2019;5:69.
[4] McCormick N, Yokose C, Challener GJ, Joshi AD, Tanikella S, Choi HK. Serum urate and recurrent gout. JAMA 2024;331:417–24.
[5] Stamp LK, Dalbeth N. Prevention and treatment of gout. Nat Rev Rheumatol 2019;15:68–70.
[6] Neilson J, Bonnon A, Dickson A, Roddy E. Gout: diagnosis and management—Summary of NICE guidance. BMJ 2022;378:o1754.
[7] Terkeltaub R. Emerging urate-lowering drugs and pharmacologic treatment strategies for gout: a narrative review. Drugs 2023;83:1501–21.
[8] Gout Mikuls TR. New England J Med 2022;387:1877–87.
[9] van Durme C.M.P.G., Wechalekar M.D., Landewé R.B., Pardo Pardo J., Cyril S., van der Heijde D., et al. Non-steroidal anti-inflammatory drugs for acute gout. Cochrane Database Syst Rev 20;16(9): CD010120.
[10] McKenzie BJ, Wechalekar MD, Johnston RV, Schlesinger N, Buchbinder R. Colchicine for acute gout. Cochrane Database Syst Rev 2021;8(8):CD006190.
[11] Liu Q, Zhang A, Wang R, Zhang Q, Cui D. A review on metal- and metal oxide-based nanozymes: properties, mechanisms, and applications. Nanomicro Lett 2021;13: 154.
[12] Ren X, Chen D, Wang Y, Li H, Zhang Y, Chen H, et al. Nanozymes-recent development and biomedical applications. J Nanobiotechnology 2022;20:92.
[13] Zhang L, Wang H, Qu X. Biosystem-inspired engineering of nanozymes for biomedical applications. Advanced Materials 2024;36(10):2211147.
[14] Zandieh M, Liu J. Nanozymes: definition, activity, and mechanisms. Advanced Materials 2024;36(10):2211041.
[15] Wang Y, Jia X, An S, Yin W, Huang J, Jiang X. Nanozyme-based regulation of cellular metabolism and their applications. Advanced Materials 2024;36(10):2301810.
[16] Zhou L, Tang S, Li F, Wu Y, Li S, Cui L, et al. Ceria nanoparticles prophylactic used for renal ischemia-reperfusion injury treatment by attenuating oxidative stress and inflammatory response. Biomaterials 2022;287:121686.
[17] Li C, Zhao Z, Luo Y, Ning T, Liu P, Chen Q, et al. Macrophage-disguised manganese dioxide nanoparticles for neuroprotection by reducing oxidative stress and modulating inflammatory microenvironment in acute ischemic stroke. Advanced Science 2021;8:2101526.
[18] Chen G, Yu Y, Fu X, Wang G, Wang Z, Wu X, et al. Microfluidic encapsulated manganese organic frameworks as enzyme mimetics for inflammatory bowel disease treatment. J Colloid Interface Sci 2022;607:1382–90.
[19] Liu Y, Cheng Y, Zhang H, Zhou M, Yu Y, Lin S, et al. Integrated cascade nanozyme catalyzes *in vivo* ROS scavenging for anti-inflammatory therapy. Sci Adv 2020;6:eabb2695.
[20] Li S, Chen Z, Wang M, Yang F, Zhang S, Qiao C, et al. Ultrasmall Cu_2O@His nanozymes with RONS scavenging capability for anti-inflammatory therapy. ACS Appl Mater Interfaces 2024;16:3116–25.
[21] Zheng J, Chen T, Wang K, Peng C, Zhao M, Xie Q, et al. Engineered multifunctional zinc–organic framework-based aggregation-induced emission nanozyme for accelerating spinal cord injury recovery. ACS Nano 2024;18:2355–69.
[22] Kuo PC, Lien CW, Mao JY, Unnikrishnan B, Chang HT, Lin HJ, et al. Detection of urinary spermine by using silver-gold/silver chloride nanozymes. Anal Chim Acta 2018;1009:89–97.
[23] Permpoka K, Purinai P, Cheerasiri C, Rojpalakorn W, Nilaratanakul V, Laiwattanapaisal W. Smartphone-enabled 3D origami-fluidic paper-based electrochemical detection of myeloperoxidase activity for assessing wound infection. Sens Actuat B: Chemical 2024;398:134712.
[24] Naveen Prasad S, Anderson SR, Joglekar MV, Hardikar AA, Bansal V, Ramanathan R. Bimetallic nanozyme mediated urine glucose monitoring through discriminant analysis of colorimetric signal. Biosens Bioelectron 2022;212:114386.
[25] Liao X, Tong W, Dai L, Han L, Sun H, Liu W, et al. Nanozyme-catalyzed cascade reaction enables a highly sensitive detection of live bacteria. J Mater Chem B 2023;11:4890–8.
[26] Wang M, Chang M, Chen Q, Wang D, Li C, Hou Z, et al. Au_2Pt-PEG-Ce6 nanoformulation with dual nanozyme activities for synergistic chemodynamic therapy /phototherapy. Biomaterials 2020;252:120093.
[27] Xu Z, Sun P, Zhang J, Lu X, Fan L, Xi J, et al. High-efficiency platinum–carbon nanozyme for photodynamic and catalytic synergistic tumor therapy. Chem Eng J 2020;399:125797.
[28] Hu Y, Wang X, Zhao P, Wang H, Gu W, Ye L. Nanozyme-catalyzed oxygen release from calcium peroxide nanoparticles for accelerated hypoxia relief and image-guided super-efficient photodynamic therapy. Biomater Sci 2020;8:2931–8.
[29] Yang J, Fang L, Jiang R, Qi L, Xiao Y, Wang W, et al. RuCu nanosheets with ultrahigh nanozyme activity for chemodynamic therapy. Adv Healthc Mater 2023;12:2300490.
[30] Liang Y, Liao C, Guo X, Li G, Yang X, Yu J, et al. RhRu Alloy-anchored MXene nanozyme for synergistic osteosarcoma therapy. Small 2023;19:2205511.
[31] Sun Y, Lu Y, Saredy J, Wang X, Drummer IV C, Shao Y, et al. ROS systems are a new integrated network for sensing homeostasis and alarming stresses in organelle metabolic processes. Redox Biol 2020;37:101696.
[32] Halliwell B. Understanding mechanisms of antioxidant action in health and disease. Nat Rev Mol Cell Biol 2024;25:13–33.
[33] Palma FR, Gantner BN, Sakiyama MJ, Kayzuka C, Shukla S, Lacchini R, et al. ROS production by mitochondria: function or dysfunction? Oncogene 2024;43:295–303.
[34] Eltzschig HK, Carmeliet P. Hypoxia and inflammation. N Engl J Med 2011;364:656–65.
[35] McGarry T, Biniecka M, Veale DJ, Fearon U. Hypoxia, oxidative stress and inflammation. Free Radical Biol Med 2018;125:15–24.
[36] Watts ER, Walmsley SR. Inflammation and hypoxia: HIF and PHD isoform selectivity. Trends Mol Med 2019;25:33–46.
[37] Jing W, Liu C, Su C, Liu L, Chen P, Li X, et al. Role of reactive oxygen species and mitochondrial damage in rheumatoid arthritis and targeted drugs. Front Immunol 2023;14:1107670.

[38] Cabău G, Crișan TO, Klück V, Popp RA, Joosten LAB. Urate-induced immune programming: consequences for gouty arthritis and hyperuricemia. Immunol Rev 2020;294:92–105.
[39] Hall CJ, Sanderson LE, Lawrence LM, Pool B, van der Kroef M, Ashimbayeva E, et al. Blocking fatty acid–fueled mROS production within macrophages alleviates acute gouty inflammation. J Clin Investigat 2018;128:1752–71.
[40] Furuhashi M. New insights into purine metabolism in metabolic diseases: role of xanthine oxidoreductase activity. Am J Physiol-Endocrinol Metabol 2020;319:E827–34.
[41] Kimura Y, Tsukui D, Kono H. Uric acid in inflammation and the pathogenesis of atherosclerosis. IJMS 2021;22:12394.
[42] Yang K, Li J, Tao L. Purine metabolism in the development of osteoporosis. Biomed Pharmacother 2022;155:113784.
[43] Dominic A, Le N-T, Takahashi M. Loop Between NLRP3 Inflammasome and reactive oxygen species. Antioxid. Redox Signal 2022;36:784–96.
[44] Bai B, Yang Y, Wang Q, Li M, Tian C, Liu Y, et al. NLRP3 inflammasome in endothelial dysfunction. Cell Death Dis 2020;11:776.
[45] Lepetsos P, Papavassiliou KA, Papavassiliou AG. Redox and NF-κB signaling in osteoarthritis. Free Radical Biol Med 2019;132:90–100.
[46] Morris G, Gevezova M, Sarafian V, Maes M. Redox regulation of the immune response. Cell Mol Immunol 2022;19:1079–101.
[47] Abu Shelbayeh O, Arroum T, Morris S, Busch KB. PGC-1α Is a master regulator of mitochondrial lifecycle and ROS stress response. Antioxidants (Basel) 2023;12:1075.
[48] Reyes-García J, Carbajal-García A, Di Mise A, Zheng YM, Wang X, Wang YX. Important functions and molecular mechanisms of mitochondrial Redox signaling in pulmonary hypertension. Antioxidants (Basel) 2022;11:473.
[49] Sun L, Wang X, Saredy J, Yuan Z, Yang X, Wang H. Innate-adaptive immunity interplay and redox regulation in immune response. Redox Biol 2020;37:101759.
[50] Dan Dunn J, Alvarez LA, Zhang X, Soldati T. Reactive oxygen species and mitochondria: a nexus of cellular homeostasis. Redox Biol 2015;6:472–85.
[51] Xi J, Zhang R, Wang L, Xu W, Liang Q, Li J, et al. A nanozyme-based artificial peroxisome ameliorates hyperuricemia and ischemic stroke. Adv Funct Mater 2021;31:2007130.
[52] Lin A, Sun Z, Xu X, Zhao S, Li J, Sun H, et al. Self-cascade uricase/catalase mimics alleviate acute gout. Nano Lett 2022;22:508–16.
[53] Dong Y, Chi Y, Lin X, Zheng L, Chen L, Chen G. Nano-sized platinum as a mimic of uricase catalyzing the oxidative degradation of uric acid. Phys Chem Chem Phys 2011;13:6319.
[54] Liu Y, Qin Y, Zhang Q, Zou W, Jin L, Guo R. Arginine-rich peptide/platinum hybrid colloid nanoparticle cluster: a single nanozyme mimicking multi-enzymatic cascade systems in peroxisome. J Colloid Interface Sci 2021;600:37–48.
[55] Liu D, Yi S, Ni X, Zhang J, Wang F, Yang P, et al. Preparation and application of nanozymes with uricase-like activity based on molecularly imprinted polymers. Chempluschem 2023;88:e202200286.
[56] Zhu S, Zeng M, Feng G, Wu H. Platinum nanoparticles as a therapeutic agent against dextran sodium sulfate-induced colitis in mice. IJN 2019;14:8361–78.
[57] Liu Y, Qing Y, Jing L, Zou W, Guo R. Platinum–copper bimetallic colloid nanoparticle cluster nanozymes with multiple enzyme-like activities for scavenging reactive oxygen species. Langmuir 2021;37:7364–72.
[58] Yan R, Sun S, Yang J, Long W, Wang J, Mu X, et al. Nanozyme-based bandage with single-atom catalysis for brain trauma. ACS Nano 2019;13:11552–60.
[59] Gao P, Wei R, Chen Y, Li X, Pan W, Li N, et al. Pt nanozyme-bridged covalent organic framework-aptamer nanoplatform for tumor targeted self-strengthening photocatalytic therapy. Biomaterials 2023;297:122109.
[60] Li X, Yang X, Cheng X, Zhao Y, Luo W, Elzatahry AA, et al. Highly dispersed Pt nanoparticles on ultrasmall EMT zeolite: a peroxidase-mimic nanoenzyme for detection of H_2O_2 or glucose. J Colloid Interface Sci 2020;570:300–11.
[61] Fu Z, Zeng W, Cai S, Li H, Ding J, Wang C, et al. Porous Au@Pt nanoparticles with superior peroxidase-like activity for colorimetric detection of spike protein of SARS-CoV-2. J Colloid Interface Sci 2021;604:113–21.
[62] Zhang L, Dong Q, Hao Y, Wang Z, Dong W, Liu Y, et al. Drug-primed self-assembly of platinum-single-atom nanozyme to regulate cellular redox homeostasis against cancer. Adv Sci (Weinh) 2023;10:e2302703.
[63] Zhu Y, Wang Z, Zhao R, Zhou Y, Feng L, Gai S, et al. Pt Decorated $Ti_3C_2T_x$ MXene with NIR-II light amplified nanozyme catalytic activity for efficient phototheranostics. ACS Nano 2022;16:3105–18.
[64] He SB, Yang L, Yang Y, Noreldeen HAA, Wu GW, Peng HP, et al. Carboxylated chitosan enabled platinum nanozyme with improved stability and ascorbate oxidase-like activity for a fluorometric acid phosphatase sensor. Carbohydr Polym 2022;298:120120.
[65] Liu Y, Wu H, Chong Y, Wamer WG, Xia Q, Cai L, et al. Platinum nanoparticles: efficient and stable catechol oxidase mimetics. ACS Appl Mater Interfaces 2015;7:19709–17.
[66] Schlesinger N, Padnick-Silver L, LaMoreaux B. Enhancing the response rate to recombinant uricases in patients with gout. BioDrugs 2022;36:95–103.
[67] Berhanu AA, Krasnokutsky S, Keenan RT, Pillinger MH. Pegloticase failure and a possible solution: immunosuppression to prevent intolerance and inefficacy in patients with gout. Semin Arthritis Rheum 2017;46:754–8.
[68] Hershfield MS, Ganson NJ, Kelly SJ, Scarlett EL, Jaggers DA, Sundy JS. Induced and pre-existing anti-polyethylene glycol antibody in a trial of every 3-week dosing of pegloticase for refractory gout, including in organ transplant recipients. Arthritis Res Ther 2014;16:R63.
[69] Jenkins C, Hwang JH, Kopp JB, Winkler CA, Cho SK. Review of urate-lowering therapeutics: from the past to the future. Front Pharmacol 2022;13:925219.
[70] Hu M, Furukawa S, Ohtani R, Sukegawa H, Nemoto Y, Reboul J, et al. Synthesis of Prussian blue nanoparticles with a hollow interior by controlled chemical etching. Angew Chem Int Ed Engl 2012;51(4):984–8.
[71] Ming H, Torad NLK, Chiang YD, Wu KCW, Yamauchi Y. Size- and shape-controlled synthesis of Prussian blue nanoparticles by a polyvinylpyrrolidone-assisted crystallization process. CrystEngComm 2012;14:3387–96.
[72] Brand DD, Latham KA, Rosloniec EF. Collagen-induced arthritis. Nat Protoc 2007;2:1269–75.
[73] Dou G, Tian R, Liu X, Yuan P, Ye Q, Liu J, et al. Chimeric apoptotic bodies functionalized with natural membrane and modular delivery system for inflammation modulation. Sci Adv 2020;6(30):eaba2987.
[74] Zhang Q, Dehaini D, Zhang Y, Zhou J, Chen X, Zhang L, et al. Neutrophil membrane-coated nanoparticles inhibit synovial inflammation and alleviate joint damage in inflammatory arthritis. Nature Nanotech 2018;13:1182–90.
[75] Gao C, Huang Q, Liu C, Kwong CHT, Yue L, Wan JB, et al. Treatment of atherosclerosis by macrophage-biomimetic nanoparticles via targeted pharmacotherapy and sequestration of proinflammatory cytokines. Nat Commun 2020;11(1):2622.

[76] Baik AH, Jain IH. Turning the oxygen dial: balancing the highs and lows. Trends Cell Biol. 2020;30:516–36.
[77] Bartz RR, Piantadosi CA. Clinical review: oxygen as a signaling molecule. Crit Care (Fullerton) 2010;14:234.
[78] Ciarlone GE, Hinojo CM, Stavitzski NM, Dean JB. CNS function and dysfunction during exposure to hyperbaric oxygen in operational and clinical settings. Redox Biol 2019;27:101159.
[79] Yan J, Jiang J, He L, Chen L. Mitochondrial superoxide/hydrogen peroxide: an emerging therapeutic target for metabolic diseases. Free Radical Biol Med 2020;152:33–42.
[80] Turrens JF. Mitochondrial formation of reactive oxygen species. J Physiol 2003;552:335–44.
[81] Salvemini D, Riley DP, Cuzzocrea S. SOD mimetics are coming of age. Nat Rev Drug Discov 2002;1(5):367–74.
[82] Yan BC, Cao J, Liu J, Gu Y, Xu Z, Li D, et al. Dietary Fe_3O_4 nanozymes prevent the injury of neurons and blood-brain barrier integrity from cerebral ischemic stroke. ACS Biomater Sci Eng 2021;7:299–310.
[83] Li L, Tovmasyan A, Sheng H, Xu B, Sampaio RS, Reboucas JS, et al. Fe porphyrin-based SOD mimic and redox-active compound, (OH)FeTnHex-2-PyP^{4+}, in a rodent ischemic stroke (MCAO) model: efficacy and pharmacokinetics as compared to its Mn analogue, (H2O)MnTnHex-2-PyP^{5+}. Antioxidants (Basel) 2020;9:E467.
[84] Petro M, Jaffer H, Yang J, Kabu S, Morris VB, Labhasetwar V. Tissue plasminogen activator followed by antioxidant-loaded nanoparticle delivery promotes activation/mobilization of progenitor cells in infarcted rat brain. Biomaterials 2016;81:169–80.
[85] Gui T, Luo L, Chhay B, Zhong L, Wei Y, Yao L, et al. Superoxide dismutase-loaded porous polymersomes as highly efficient antioxidant nanoparticles targeting synovium for osteoarthritis therapy. Biomaterials 2022;283:121437.
[86] Huang G, Zang J, He L, Zhu H, Huang J, Yuan Z, et al. Bioactive nanoenzyme reverses oxidative damage and endoplasmic reticulum stress in neurons under ischemic stroke. ACS Nano 2022;16:431–52.
[87] Yang B, Yao H, Yang J, Chen C, Shi J. Construction of a two-dimensional artificial antioxidase for nanocatalytic rheumatoid arthritis treatment. Nat Commun 2022;13:1988.
[88] Bai S, Shao X, Tao Y, Wang S, Han H, Li Q. Superoxide dismutase-embedded metal-organic frameworks via biomimetic mineralization for the treatment of inflammatory bowel disease. J Mater Chem B 2022;10:5174–81.
[89] Guo H, Guo H, Xie Y, Chen Y, Lu C, Yang Z, et al. Mo_3Se_4 nanoparticle with ROS scavenging and multi-enzyme activity for the treatment of DSS-induced colitis in mice. Redox Biol 2022;56:102441.
[90] Zhang G, Han S, Wang L, Yao Y, Chen K, Chen S. A ternary synergistic eNOS gene delivery system based on calcium ion and L-arginine for accelerating angiogenesis by maximizing NO production. IJN 2022;17:1987–2000.
[91] Jenkins C, Hwang JH, Kopp JB, Winkler CA, Cho SK. Review of urate-lowering therapeutics: from the past to the future. Front Pharmacol 2022;13:13.
[92] Liu L, Zhu L, Liu M, Zhao L, Yu Y, Xue Y, et al. Recent insights into the role of macrophages in acute gout. Front Immunol 2022;13:955806.
[93] So AK, Martinon F. Inflammation in gout: mechanisms and therapeutic targets. Nat Rev Rheumatol 2017;13:639–47.
[94] Van den Bossche J, O'Neill LA, Menon D. Macrophage immunometabolism: where are we going? Trends Immunol. 2017;38:395–406.
[95] Barclay AN, van den Berg TK. The Interaction between signal regulatory protein Alpha (SIRPα) and CD47: structure, function, and therapeutic target. Annu Rev Immunol 2014;32:25–50.
[96] Vladimirova YV, Mølmer MK, Antonsen KW, Møller N, Rittig N, Nielsen MC, et al. A new serum macrophage checkpoint biomarker for innate immunotherapy: soluble signal-regulatory protein Alpha (sSIRPα). Biomolecules 2022;12:937.
[97] Greenwood J, Wang Y, Calder VL. Lymphocyte adhesion and transendothelial migration in the central nervous system: the role of LFA-1, ICAM-1, VLA-4 and VCAM-1. off. Immunology 1995;86:408–15.
[98] Boscacci RT, Pfeiffer F, Gollmer K, Sevilla AIC, Martin AM, Soriano SF, et al. Comprehensive analysis of lymph node stroma-expressed Ig superfamily members reveals redundant and nonredundant roles for ICAM-1, ICAM-2, and VCAM-1 in lymphocyte homing. Blood 2010;116:915–25.
[99] Yan Y, Jiang W, Spinetti T, Tardivel A, Castillo R, Bourquin C, et al. Omega-3 fatty acids prevent inflammation and metabolic disorder through inhibition of NLRP3 inflammasome activation. Immunity 2013;38:1154–63.
[100] He H, Jiang H, Chen Y, Ye J, Wang A, Wang C, et al. Oridonin is a covalent NLRP3 inhibitor with strong anti-inflammasome activity. Nat Commun 2018;9:2550.
[101] Huang Y, Jiang H, Chen Y, Wang X, Yang Y, Tao J, et al. Tranilast directly targets NLRP 3 to treat inflammasome-driven diseases. EMBO Mol Med 2018;10(4):e8689.
[102] Schauer C, Janko C, Munoz LE, Zhao Y, Kienhöfer D, Frey B, et al. Aggregated neutrophil extracellular traps limit inflammation by degrading cytokines and chemokines. Nat Med 2014;20:511–17.
[103] Wu M-M, Wang QM, Huang BY, Mai CT, Wang CL, Wang TT, et al. Dioscin ameliorates murine ulcerative colitis by regulating macrophage polarization. Pharmacol Res 2021;172:105796.
[104] Lee YZ, Guo HC, Zhao GH, Yang CW, Chang HY, Yang RB, et al. Tylophorine-based compounds are therapeutic in rheumatoid arthritis by targeting the caprin-1 ribonucleoprotein complex and inhibiting expression of associated c-Myc and HIF-1α. Pharmacol Res 2020;152:104581.
[105] Li Y, Liang Q, Zhou L, Cao Y, Yang J, Li J, et al. An ROS-responsive artesunate prodrug nanosystem co-delivers dexamethasone for rheumatoid arthritis treatment through the HIF-1α/NF-κB cascade regulation of ROS scavenging and macrophage repolarization. Acta Biomater 2022;152:406–24.
[106] Wu Mian, Zhang M, Ma Y, Liu F, Chen S, Lu J, et al. Chaetocin attenuates gout in mice through inhibiting HIF-1α and NLRP3 inflammasome-dependent IL-1β secretion in macrophages. Arch Biochem Biophys 2019;670:94–103.
[107] Jun CD, Shimaoka M, Carman CV, Takagi J, Springer TA. Dimerization and the effectiveness of ICAM-1 in mediating LFA-1-dependent adhesion. Proc Natl Acad Sci USA 2001;98(12):6830–5.
[108] Lynam E, Sklar LA, Taylor AD, Neelamegham S, Edwards BS, Smith CW, et al. β_2-integrins mediate stable adhesion in collisional interactions between neutrophils and ICAM-1-expressing cells. J Leukoc Biol 1998;64:622–30.
[109] Chen X, Wong R, Khalidov I, Wang AY, Leelawattanachai J, Wang Y, et al. Inflamed leukocyte-mimetic nanoparticles for molecular imaging of inflammation. Biomaterials 2011;32:7651–61.
[110] Rothenbacher D, Primatesta P, Ferreira A, Cea-Soriano L, Rodríguez LAG. Frequency and risk factors of gout flares in a large population-based cohort of incident gout. Rheumatology (Oxford) 2011;50:973–81.